

Research Article

A Combined Experimental and First-Principle Calculation (DFT Study) for In Situ Polymer Inclusion Membrane-Assisted Growth of Metal-Organic Frameworks (MOFs)

Reza Darvishi  and Esmail Pakizeh 

Faculty of Petroleum and Gas, Yasouj University, Gachsaran 75813-56001, Iran

Correspondence should be addressed to Reza Darvishi; r.darvishi@yu.ac.ir

Received 6 January 2020; Revised 17 March 2020; Accepted 23 April 2020; Published 5 June 2020

Academic Editor: Anjanapura V. Raghu

Copyright © 2020 Reza Darvishi and Esmail Pakizeh. This is an open access article distributed under the Creative Commons Attribution License, which permits unrestricted use, distribution, and reproduction in any medium, provided the original work is properly cited.

A simple yet effective strategy was developed to prepare a metal-organic framework- (MOF-) based asymmetric membrane by depositing the Zeolitic imidazolate framework-8 (Zif-8) layer on the aminosilane-functionalized surface of a polymer inclusion membrane via an in situ growth process. During the extraction of the ligand molecules from the source to stripping compartment, metal ions react with ligand, and layers of Zif-8 were gradually grown onto aminosilane-modified polymer inclusion membrane (PIM). The properties of the surface-grown Zif-8 nanocrystalline layer were well characterized by powder X-ray diffraction, adsorption-desorption analysis, and scanning electron microscopy. The potential use of these Zif-8-supported PIM membranes for the separation of gases N_2 , CH_4 , and CO_2 was evaluated at two temperatures (25 and 50°C) and pressures (1, 3, and 5 bar), by comparing the permeability and selectivity behavior of these membranes with neat PIM. The gas permeability of both pure PIM ($P_{CO_2} = 799.2$ barrer) and PIM-co-MOF ($P_{CO_2} = 675.8$ barrer) increases with the temperature for all three gases, and the permeation rate order was $CO_2 > CH_4 > N_2$. The results showed that the presence of a layer of Zif-8 on the surface of the polymer inclusion membranes can get a slightly reduced permeability (~21%) but an enhanced selectivity of up to ~70% for CO_2/CH_4 and ~34% for CO_2/N_2 . In the case of both membrane types, the ideal permselectivity decreases with the temperature, but this decrease was slightly more pronounced for the case of PIM-co-MOF. To understand more details about the electronic structure and optical and adsorption properties of Zif-8 and $M+Zif-8$ ($M = N_2, CH_4, \text{ and } CO_2$) compounds, the periodic plane-wave density functional theory (DFT) calculations were used. The electronic band structures and density of states for pure Zif-8 showed that this compound is metallic. Also, using DFT, the formation energy of $M+Zif-8$ compounds was calculated, and we showed that the $CO_2+Zif-8$ composition is more stable than other compounds. This result suggests that the tendency of the Zif-8 compound to absorb the CO_2 molecule is higher than that of other molecules. Confirming these results, DFT optical calculations showed that the affinity of the $CO_2+Zif-8$ composition to absorb infrared light was greater than that of the other compounds.

1. Introduction

Membrane technology has been widely applied across various industries, such as medication (blood fractionation), purification and desalination of water, and gas and mixture separation [1–7]. Membrane gas separation has the potential for applications such as oxygen enrichment, nitrogen generation, hydrogen recovery, and carbon dioxide removal [7, 8]. However, the growth of the gas separation membranes market in recent years is attributed to the increasing demand for

carbon dioxide removal applications [8–11]. The development of a potential polymer is key to any further research in the gas separation membrane [7]. Over the past few decades, many polymers have been studied for gas membrane applications, but only relatively few polymers have been established as common gas separation membranes [7, 9, 12]. Polymers for gas separation processes have to meet several requirements simultaneously, such as rapid mass transfer rate and high selectivity towards a specific gas, the ability to easily form desired membrane

configurations, and resistance to swelling induced plasticization. The aim of the development of new material is to combine high permeability with high permselectivity [8–11, 13]. Polymer inclusion membranes (PIMs) and metal-organic frameworks (MOFs) have been investigated for membrane applications which are of potential interest in gas recycling and recovery applications [13, 14]. MOFs have been introduced as novel fillers for incorporation in many different polymer matrices to form composite or mixed-matrix membranes (MMMs) for achieving good permeability and high selectivity [10, 15]. Rodenas et al. [16] studied the NH₂-MIL-53(Al)-filled polyimide-based MMMs and reported that the stability, selectivity, and permeability for CO₂/CH₄ separation are more enhanced compared with unfilled membranes. In principle, highly permeable MOFs have drawbacks in terms of brittleness and lack of flexibility, hindering their fabrication into continuous sheets and thus limiting their usage for further practical application. The drawbacks can be overcome by incorporating them into the polymer matrix. However, most of the polymers are incompatible with the MOF particles and are difficult to achieve uniform dispersion of the MOF in the MMMs [4, 10, 15–18]. The lack of strong interface between the MOF and polymer can cause the formation of agglomeration of the particles and nonselective interfacial voids. On the other side, high filler loadings can result in a brittle and rigid behavior of MMMs and a reduction of mechanical properties. Besides these issues, the polymer chains can penetrate the pores of MOF fillers, partially blocking the pore entrance and thus reducing gas permeability of the membranes [15, 17, 19].

Polymer inclusion membranes (PIMs), a dense carrier-mediated transport membrane, are widely used for selectively recovering a target solute from a complex mixture. They are a type of self-supported liquid membranes in which extraction and stripping can be carried out in one operation with high selectivity for ion transport [3, 4]. These membranes are easy to fabricate and have outstanding mechanical properties. PIMs consist of a polymer, a plasticizer, and a carrier molecule facilitating the transport of both organic and inorganic species. The polymer support provides mechanical strength, the plasticizer improves flexibility, and the liquid phase facilitates the mobility of the carrier molecule. The carrier molecule acts as a guest-specific host, which can bound to target species by noncovalent intermolecular interactions, such as van der Waals, hydrophobic, or hydrogen bonds, thereby providing selective membrane permeability for target species [3]. Kebiche-Senhadjji et al. [15] studied the pure gas permeation behavior of a CTA-based PIM containing an acidic carrier and found that gas permeation and CO₂/H₂ permselectivity increases during the incorporation of the plasticizer and acidic carrier into the CTA.

This paper proposes a new approach for developing an asymmetric composite membrane, by growing Zeolitic imidazolate framework (Zif-8) particles on the surface of a novel polymer inclusion membranes, which were shown in a previous work to be efficient in facilitating transport of calcium cations [4]. For enhancing the adhesion between PIM support and Zif-8 particles, the surface modification of the solid

substrate was performed through the reaction between an aminosilane compound and free hydroxyl groups on the polymer backbone [4]. A comparative study of gas transport through two types of membranes (pure PIM and Zif-8-coated PIM (coded as PIM-co-MOF)) was performed to evaluate more precisely the effect of the deposited Zif-8 crystal layer on membrane performance. The electronic band structures and density of states for the Zif-8 layer were also calculated using first-principles based on the density functional theory (DFT). Also, the optical and adsorption properties of Zif-8 and M+Zif-8 ($M = N_2, CH_4, \text{ and } CO_2$) were calculated with DFT, and their results are in agreement with the experimental data. The observations showed that the new class of the PIM-co-MOF membrane is more flexible compared to high-MOF-content MMMs. Although there are many different in situ synthesis techniques to directly grow/deposit the different types of MOF of solid surfaces [20–24], to our knowledge, there is no work reported in the literature concerning the usage of PIMs as support for in situ synthesis of MOFs on the membrane surfaces, and there are only very few studies that utilized PIMs for in situ synthesis of metal nanoparticles applications [25]. The growth of Zif-8 nanoparticles onto polymer inclusion membranes has the potential to convert them to the high-quality membrane for different applications. The prepared PIM-co-MOF was studied utilizing X-ray diffraction (XRD), Fourier transforms infrared spectroscopy (FTIR), scanning electron microscopy (SEM), and Brunauer–Emmett–Teller (BET) surface area. It will be expected that the proposed method can be considered as an alternative technique for MOF and novel hybrid MOF-coated membranes fabrication with additional selectivity through which the application of MOFs could be extended in the area such as filtration, sensors, and even ion and gas separation.

2. Experimental

2.1. Material. Cellulose acetate (CA, degree of acetylation: 2.87 and molecular weight: ~78,000 g/mole), isophorone diisocyanate, Benzo18Crown6, and ionic liquid, 1-butyl-3-methyl-imidazolium chloride ([BMIM] [Cl]), were bought from Sigma-Aldrich. Castor oil, (iodine value 90, viscosity of 950–1050 mPa·s at 20°C) was purchased from M/s SD Fine-Chem Limited, Mumbai, India. N,N-Dimethylacetamide (DMAC), zinc nitrate hexahydrate, and 2-methyl imidazole were provided by the Merck company. All chemicals were used as received.

2.2. Characterization. Nitrogen adsorption-desorption isotherms were obtained using a Micromeritics ASAP-2020 instrument at 77 K to measure pore textural properties of the synthesized Zi-8 samples. The X-ray diffraction (XRD) measurements were obtained using a STOE STADI MP (Germany) diffractometer (40 kV, 30 mA) with CuK α ($\lambda = 1.54184 \text{ \AA}$) source radiation at room temperature. The scanning rate was 2°/min in the range of 5° to 70° and a count time of 0.1 s/step. Fourier transform infrared (FTIR) spectra were recorded using a Bruker Vector 22, a German spectrophotometer equipped with a KBr beam splitter, with a

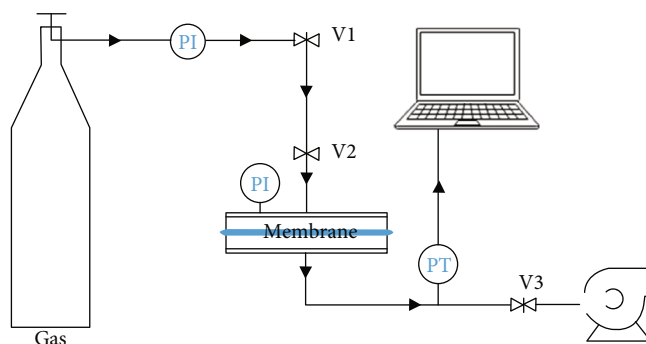


FIGURE 1: Schematic of the experimental setup for gas separation test.

wavenumber range of 4000 to 500 cm^{-1} at a resolution of 6 or 4 cm^{-1} . Scanning electron microscopy (ZEISS EVO18) was used to study the quality and morphology of produced PIM and PIM-co-Zif-8. The samples were frozen in liquid nitrogen and then were mechanically broken into pieces. Then, the fractured samples were coated with a thin layer of gold using a gold sputterer (model SCD005, Bal-Tec, Hannover, Germany) in a vacuum, and then micrographs were prepared.

2.3. Preparation and Modification of PIM. In the present work, we modified the novel PIM, which was fabricated and characterized in the previous work in detail [4]. In brief, the PIM membrane was prepared by casting the solution of GPO which in turn synthesized by a reaction between epoxidized castor oil and cellulose acetate, thereafter, cross-linked by isophorone diisocyanate, crown ether, and ionic liquid in dimethylacetamide (DMAc) on an immaculate glass using a knife (Doctor Blade). The prepared dry PIM was configured into a two-compartment glass cell for the feed and stripping phases with 200 cm^3 volume each. A 5 cm diameter PIM was sandwiched between the circular openings of the two compartments. 3-Aminopropyl trimethoxysilane was dissolved in the feed chamber at a concentration of 5% , and pH was adjusted to 4.5 by adding some 0.1 M hydrochloric acid solution. The stripping aqueous phase consisted of distilled deionized water. The cells were gently stirred for 24 h at 25°C (50 rpm). Finally, the membranes were washed three times with water.

2.4. ZIF-8 Deposition on PIM Surface. In this work, an in situ PIM-assisted growth method has been developed for the synthesis of metal-organic frameworks (MOFs) Zif-8 on the amino-functionalized membrane surface. In this procedure, the amino-functionalized PIM clamped between the two compartments of the above-described diffusion cell. The feed phase was homogenized by stirring at a speed of 500 rpm with a magnetic bar. The feed compartment was filled with an aqueous solution containing the 5 mg of zinc nitrate hexahydrate, and the receiving compartment was filled with an aqueous solution containing 20 mg of 2-methylimidazole. The extraction of Zn(II) into the PIM was carried out for a predetermined period of time at 25°C . This PIM-supported Zif-8 membrane is called PIM-co-MOF from here on.

2.5. Measurement of Gas Permeability. The gas permeation properties of both membranes of neat PIM and PIM-co-MOF were measured in a constant volume/variable pressure gas permeability apparatus (Figure 1) at controlled temperature and pressure. Single gas permeability values of N_2 , CO_2 , and CH_4 at 298 K and 323 K and pressures of 1 , 3 , and 5 bar were obtained.

The gas permeability was calculated using the following equation [9]:

$$P = \frac{273.15 \times 10^{10}}{760AT} \times \frac{14.7VL}{P_0 \times 76} \times \frac{dp}{dt}, \quad (1)$$

where P is the gas permeability (barrer), V is the downstream volume (cm^3), L is the membrane thickness (cm), A is the effective area of the membrane (cm^2), T is the operating temperature (K), P_0 is the feed gas pressure (psi), and dp/dt is the steady rate of pressure increase in the downstream side (cmHg/sec). The ideal permselectivity between two different gases is defined as the ratio of the single gas permeabilities and determined as [26]:

$$\alpha = \frac{P_A}{P_B}. \quad (2)$$

3. Computational Methods and Model Systems

In this paper, the calculations were performed using the density functional theory and Quantum ESPRESSO package [27]. The exchange-correlation term was considered within the generalized gradient (GGA) approximation presented by Perdew–Burke–Ernzerhof (PBE) [28]. The energy cut-off for the extension of the wave-functions was selected as 408 eV . The Brillouin zone integration was executed over a Monkhorst–Pack $4 \times 4 \times 4$ meshes [29]. The lattice constant of the Zif-8 material was optimized until the total energy converged to at least 10^{-3} eV . In the theoretical calculations, the unit cells of Zif-8 with cubic structure and space group ($I-43m$) are shown in Figure 2.

In this figure, each central zinc (Zn) element is coordinated by four 2-methylimidazolate ligands with one of its two N atoms. To simulate the Zif-8 compound, we used a unit cell with 156 atoms and $\text{Zn}_{12}\text{N}_{48}\text{C}_{48}\text{H}_{48}$ formula. The

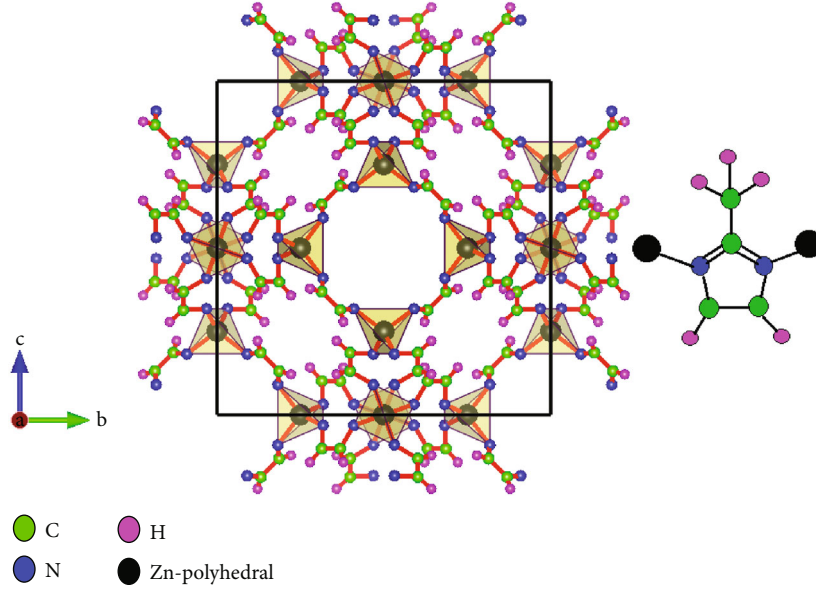


FIGURE 2: Top views of the atomic structure of the Zif-8 compound. The green, blue, pink, and black spheres represent C, N, H, and Zn atoms, respectively.

TABLE 1: Atomic position of Zn in Zif-8 compounds.

Atoms	X (Å)	Y (Å)	Z (Å)
Zn ₁	12.74	0	8.49
Zn ₂	8.49	4.24	0
Zn ₃	8.49	12.74	0
Zn ₄	4.24	0	8.49
Zn ₅	0	8.49	4.24
Zn ₆	0	12.74	8.49
Zn ₇	12.74	8.49	0
Zn ₈	0	4.24	8.49
Zn ₉	4.24	8.49	0
Zn ₁₀	0	8.49	12.74
Zn ₁₁	8.49	0	4.24
Zn ₁₂	8.49	0	12.74

atomic positions of Zn in this structure are presented in Table 1.

Also, the optimized structure parameters of Zif-8 compounds are shown in Table 2.

4. Theory Results and Discussion

4.1. Electronic Band Structure and Density of States. The electronic band structure and partial density of states (PDOS) of Zif-8 compounds are shown in Figures 3(b) and 3(c), respectively.

Figure 3(a) also shows the band structure in the range of -0.6 to 0.4 eV for more clarity. To help readability, we used a color legend for the DOS. We drew in black, green, blue, and red colors the total, p, d, and s DOS, respectively. To specify the metallic systems, the Fermi energy (E_F) was taken here as the highest occupied energy level of the system. The symmetry points, while in the cubic

TABLE 2: Calculated bond lengths, bond angle, and lattice constants of Zif-8.

ZN-N (Å)	1.99	N-Zn-N (°)	109.44
N-C (Å)	1.37	Zn-N-C (°)	126.52
C-C (Å)	1.32	N-C-H (°)	125.56
C-H (Å)	0.93	H-C-C (°)	125.55
$a = b = c$ (Å)	16.99	$\alpha = \beta = \gamma$ (°)	90

Brillouin zone (BZ) in which Zif-8 compound crystallizes, are plotted in Figure 4. Coordinates of the k points within a cubic BZ framework are following: Γ (0 0 0), X (0.5 0 0), M (0.5 0.5 0), and R (0.5 0.5 0.5) [30].

The set of atomic electron configurations included in the present band structure computation process of Zif-8 is listed in Table 3.

According to Figures 3(a) and 3(b), the band structure crosses the Fermi level (E_F) at various symmetry directions, suggesting a metallic-like character of Zif-8 compounds. The electronic bands are mostly found in the energy range of -1.3 to -3 eV, due to the dispersive nature of p orbitals of Zn and N atoms. Low allowed energy states in the valence region of Figure 3(c) are mainly originated due to s orbitals with a small contribution. Due to the type of occupation of atomic orbitals by electrons, the highest density of states is related to the p orbitals of the Zn, N, and C atoms. When the semi-core electrons are omitted, the d bands are shifted up while the sp bands are shifted down in a nonhomogeneous way. This leads to a reduction of the d-sp interband gap in the range of -1 to 0.5, -4 to -3, and -5.4 to -4.7 eV [31]. This result is quite clear in Figure 3(b).

4.2. Adsorption Properties. The formation energy or enthalpy of formation shows the thermodynamic stability of the materials [32]. Under ideal conditions (zero Kelvin temperature

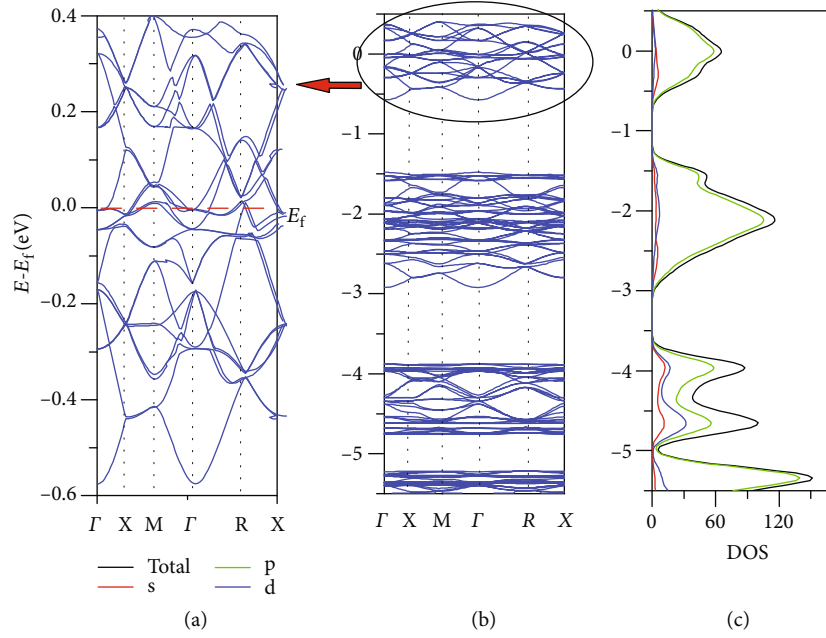


FIGURE 3: The calculated electronic band structure and density of states (DOS) of Zif-8 compounds.

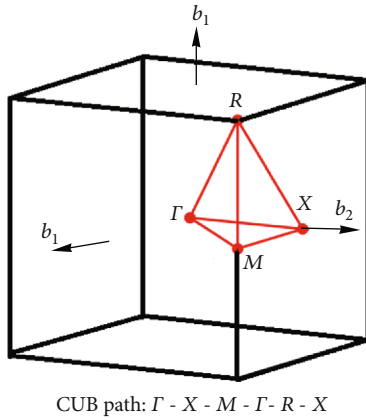


FIGURE 4: The high symmetry k -path in the cubic first Brillouin zone.

and zero pressure) for the first time, we calculated the formation energy of M +Zif-8 ($M = N_2, CH_4,$ and CO_2) compounds. The locations of dope M molecules to calculate the formation energy of M +Zif-8 are shown in Figure 5 (near the red Zn polyhedral).

For each case in the unit cell, four M molecules were used. In the experimental section, the adsorption of M molecules by Zif-8 is investigated, and there we showed that the adsorption of M molecules is done by zinc elements, so they are located near the Zn atoms in the simulation part. The formation energy (E_F) of compounds is calculated as

$$E_F = \frac{E(xM + Zif8) - E(Zif8) - xE(M)}{x}, \quad (3)$$

where x is the number of doped atoms ($M = N_2, CH_4,$ and CO_2), $E(xM + Zif - 8)$, $E(Zif - 8)$, and

TABLE 3: Atomic orbitals as employed in the present band structure computation of Zif-8.

Element	Core electrons	Semi-core electrons	Valence electrons
Zn	$1s^2 2s^2 2p^6$	$3s^2 3p^6$	$4s^2 3d^{10}$
N	$1s^2$	$2s^2$	$2p^3$
C	$1s^2$	$2s^2$	$2p^2$
H	—	—	$1s^1$

$E(M)$ the total energy of M +Zif-8, Zif-8, and M molecules, respectively. This energy reflects the stability of the compounds. The total and formation energies of compounds are shown in Table 4.

According to this table, on comparing the formation energies between compounds, the minimum formation energy was evaluated to be -14.6 eV in the Zif-8+ CO_2 case. This indicates that the tendency of the Zif-8 compound to adsorption of CO_2 molecules is greater than in other cases.

4.3. Optical Properties. In this work, we used generalized gradient approximation (GGA) in the framework of DFT to calculate the optical properties of Zif-8 and M +Zif-8 compounds. These properties include real and imaginary parts of the dielectric function, extinction parameter, and adsorption coefficient. The optical properties are related to the frequency-dependent complex dielectric function $\epsilon(\omega)$ by the following relation [33]:

$$\epsilon(\omega) = \epsilon_1(\omega) + i\epsilon_2(\omega), \quad (4)$$

where $\epsilon_1(\omega)$ and $\epsilon_2(\omega)$ are the real and imaginary parts of dielectric function, respectively. The real part is related to

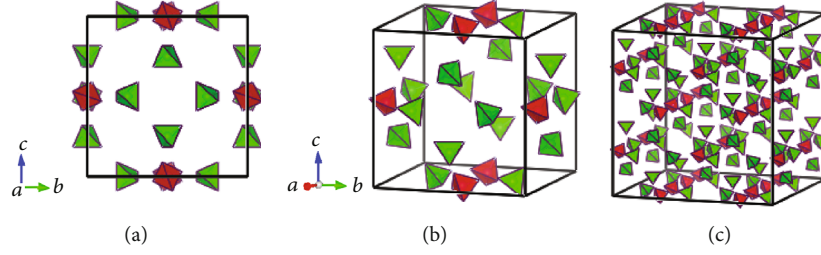


FIGURE 5: The location of M molecules in the Zif-8 compound. (a) Top view of unit cell. (b) Crystal shape view of unit cell. (c) Crystal shape of $2 \times 2 \times 2$ super cell.

TABLE 4: Total and formation energies of M +Zif-8 compounds.

Materials	Zif-8-N ₂	Zif-8-CH ₄	Zif-8-CO ₂
Total energy (eV)	-41862.60	-40571.92	-43793.53
Formation energy (eV)	-12.39	-9.05	-14.60

the electronic polarizability of the compounds, and the imaginary part is related to the electronic absorption of the compounds. The imaginary part of dielectric function can be defined as [34]:

$$\varepsilon_2(\omega) = \frac{2\pi e^2}{\Omega \varepsilon_0} \sum_{k,v,c} |\langle \Psi_k^c | u \cdot r | \Psi_k^v \rangle|^2 \delta(E_k^c - E_k^v - E) \quad (5)$$

where Ω is the volume of the unit cell, e indicates electronic charge, ε_0 signifies permittivity of free space, u defines the polarization of the incident electric field, r and k are the vectors in the real and reciprocal lattice, respectively, and Ψ_k^c and Ψ_k^v are the valence band and conduction band wavefunctions at k point corresponding to energies E_k^c and E_k^v , respectively. The $\varepsilon_1(\omega)$ and $\varepsilon_2(\omega)$ parameters are related to each other using the famous Kramer-Kronig transformations [35–37]. These relations are used to obtain the real part of dielectric function from the imaginary part. From $\varepsilon_1(\omega)$ and $\varepsilon_2(\omega)$, the other optical constants such as the extinction coefficient $k(\omega)$ and adsorption coefficient $A(\omega)$ can be determined as follows [33]:

$$k(\omega) = \sqrt{1/2 \left\{ \sqrt{(\varepsilon_1(\omega)^2 + \varepsilon_2(\omega)^2)} - \varepsilon_1(\omega) \right\}}, \quad (6)$$

$$A(\omega) = \frac{2k(\omega)E}{\hbar c}. \quad (7)$$

The calculated optical parameters were evaluated in the energy range of 0 to 5 eV (infrared–visible–ultraviolet ranges). The schematic plots of $\varepsilon_1(\omega)$ and $\varepsilon_2(\omega)$ of Zif-8 and M +Zif-8 compounds are shown in Figure 6.

The real part $\varepsilon_1(\omega)$ of the dielectric function shows the lowest peak intensity at 0.44, 0.41, 0.45, and 0.67 eV for Zif-8+CH₄, Zif+CO₂, Zif-8, and Zif-8+N₂, respectively. The imaginary part $\varepsilon_2(\omega)$ shows the energy peaks at about 0.13 eV for the Zif-8+CO₂ and Zif-8+N₂ and 0.14 eV for the Zif-8 and Zif-8+CH₄ compounds. These peaks belong to the electronic transition from Zn 3d to N and C 2p states at the

conduction and valence band. The adsorption coefficient $A(\omega)$ of compounds is presented in Figure 7.

This parameter occurs in the infrared light region at an adsorption edge from 0 to 1.5 eV. The prominent peaks intensity for adsorption values of Zif-8+CO₂, Zif+N₂, Zif-8+CH₄, and Zif-8 compounds are 18.43×10^4 , 14.77×10^4 , 13.55×10^4 , and $13.30 \times 10^4 \text{ cm}^{-1}$ corresponding to the energy peak at 0.79, 0.61, 0.57, and 0.70 eV, respectively. Therefore, Zif-8+CO₂ is chosen for optical infrared applications due to its higher adsorption coefficient [38–40].

5. Experimental Results and Discussion

5.1. Analysis of PIM-co-MOF. Since the GPO molecules, in which the membrane is made from, has hydroxyl groups on its branches, the membrane surface is full of hydroxyl functional groups that can be used for subsequent reactions. The hydroxyl groups on the membrane surface can react with APTS molecules through a very slow alcohol exchange/hydrolysis reaction. Therefore, the side of the membrane that is exposed to the APTS solution will be functionalized with aminosilane groups. This fact can also be confirmed by comparing their FTIR spectra of the aminosilane-functionalized PIM with the spectra in bare PIM as shown in Figure 8.

The samples were used for the FTIR tests and the characteristic spectra were scanned in the wavenumber range of 4000 to 500 cm^{-1} using KBr pellets. It could be observed that, compared with the unmodified membrane, the aminosilane-coated PIM possess adsorption band in 1091.5 cm^{-1} due to the stretching vibration of the C-N bond, band in 1051.0 cm^{-1} due to the stretching vibration of Si-O bond, band in 885.2 cm^{-1} due to the bending vibration of NH group, and band near 3400 cm^{-1} due to the NH₂ group. All of these reveal that the PIM was functionalized successfully with aminosilane molecules; thus, this approach can be considered as an alternative route for the aminosilane functionalization of membranes.

The next step for the experiment will be to grow Zif-8 particles on the modified surface of the membrane where the membranes were clamped between the receiving (methyl imidazole) and feed solution (zinc nitrate) compartments. Because of the presence of crown ether in the membrane and hydrophobic characteristic of the membrane, methyl imidazole molecules pass through much more rapidly than Zinc(II) ions. Imidazole molecules can gradually move from one side of the membrane to the other and react with

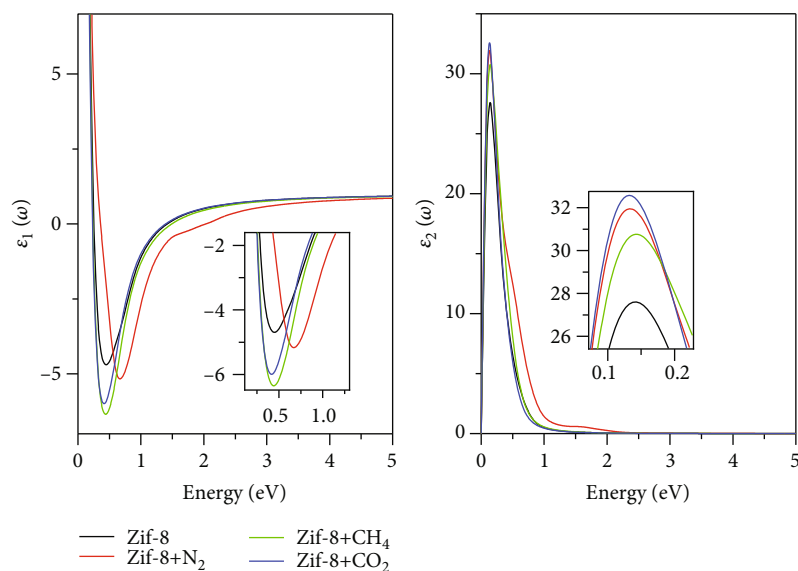


FIGURE 6: Real $\epsilon_1(\omega)$ and imaginary $\epsilon_2(\omega)$ parts of the dielectric function.

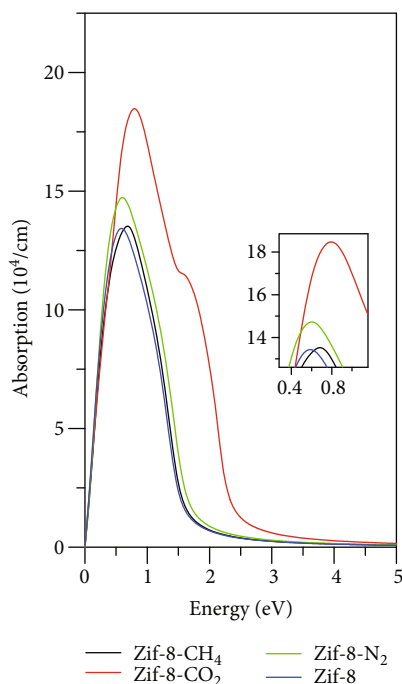


FIGURE 7: The adsorption coefficient of Zif-8 and $M+Zif-8$ compounds.

performed zinc clusters on the membrane surface. Therefore, MOF particles are formed on the side contacted with zinc nitrate solution. The crystal morphology of Zif-8 grown on the PIM is shown by virtue of FESEM. Figure 9 shows the SEM images of the PIM surface before and after MOF deposition. Under this circumstance, the whole surface of PIM was covered with continuous rod-like crystals of Zif-8 after 1^oh.

The aminosilane-functionalized PIM shares the amine functionality of the PIM building block as anchoring in Zif-8 and allows the MOF clusters to grow.

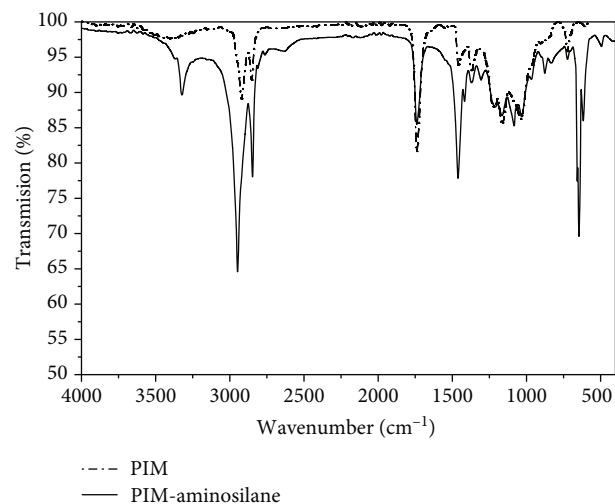


FIGURE 8: FTIR of amino silane-modified polymer inclusion membrane.

For deeply understanding the role of aminosilane, a control experiment was performed with a PIM with the same composition and without any aminosilane functionalization. Under this circumstance, Zif-8 crystals grew in a discrete stratum upon membrane and removed after being washed several times with methanol/water (the images are not shown here). Moreover, the weight percentage of Zif-8 adhered to the surface of the aminosilane-modified PIM was much higher (23 wt%) compared to that for bare PIM (only 4.3 wt%). It implies the presence of the hydroxyl pendant group upon GPO chains can also share the MOF crystal formation but NH_2 groups facilitate efficient nucleation and could better contribute to Zif-8 crystal formation than OH groups.

Figure 10 exhibits the cross-sectional SEM images of the membranes, PIM and PIM-co-MOF.

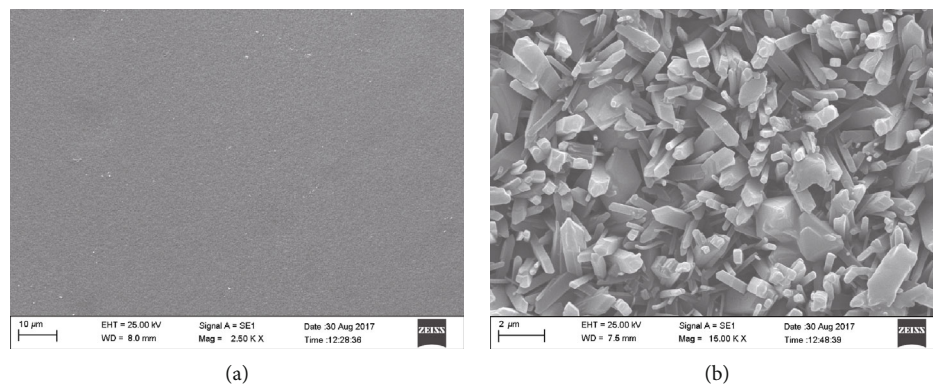


FIGURE 9: SEM images of the PIM surfaces of before (a) and after (b) Zif-8 deposition.

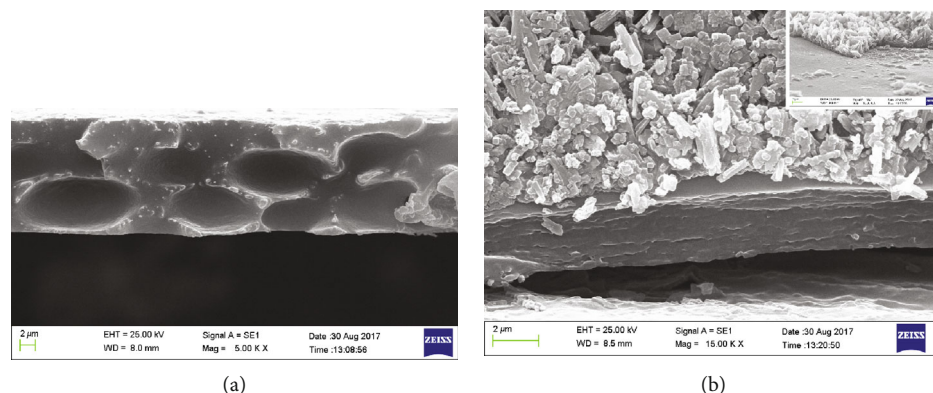


FIGURE 10: Cross-section of the membranes: (a) neat PIM and (b) PIM-co-MOF.

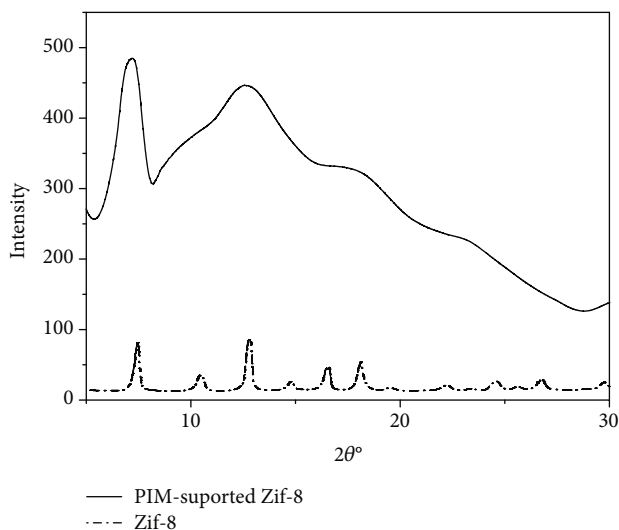


FIGURE 11: XRD spectra of Zif-8 deposited on the PIM surface.

The cross-section of the PIM-co-MOF membrane indicates that the Zif-8 thin films are composed of 1 μm thickness layer of closely intergrown nano-sized crystals that tightly adhere to the surface of the PIM support (Figure 10).

There is no gap between the Zif-8 nanoparticles layer and PIM support, once again indicating good interface adhesion

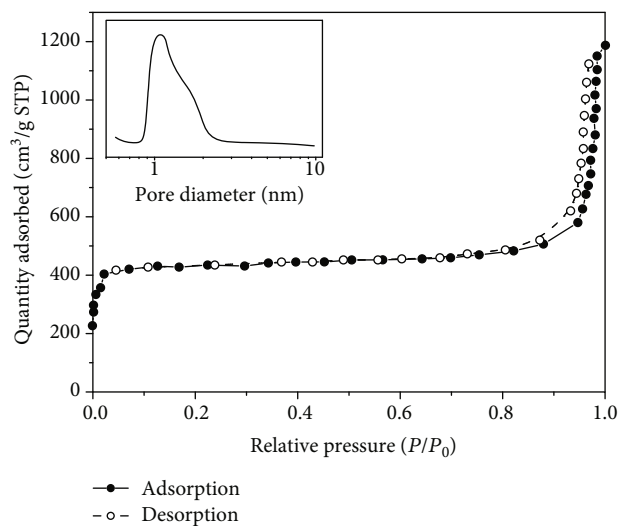


FIGURE 12: N_2 adsorption-desorption isotherms of the Zif-8 supported PIM.

between the PIM support and Zif-8 particles. The X-ray diffraction pattern of the PIM-co-MOF membrane is also shown in Figure 11.

The peak at 8.84° , characteristic of the simulated Zif-8, is clearly visible in the XRD pattern, confirming the presence of Zif-8 on the PIM. Nitrogen adsorption-desorption analysis

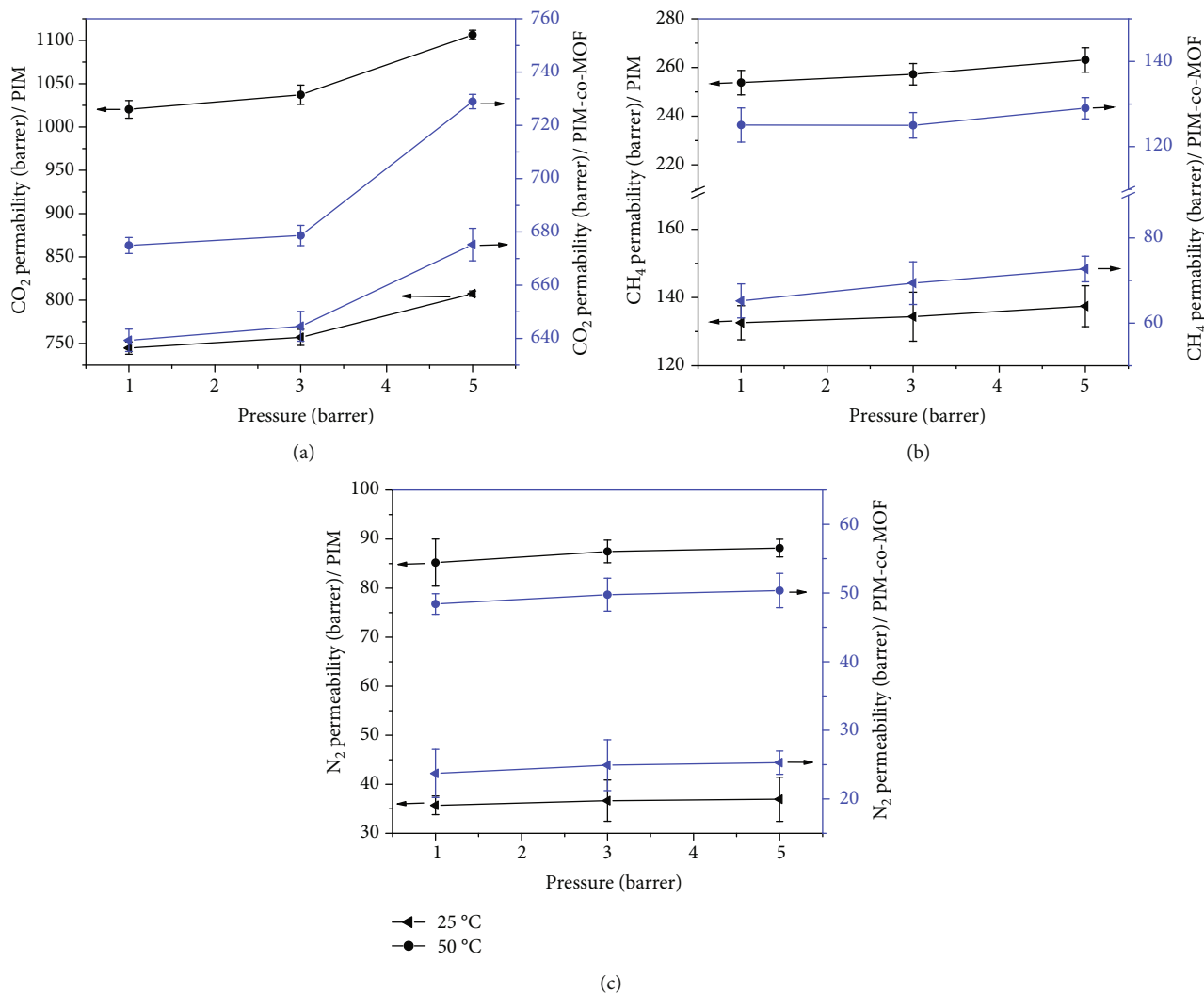


FIGURE 13: The permeability of the PIM and PIM-co-MOF as a function of feed pressure.

and pore size distribution were carried out to evaluate the pore sizes and surface area properties of PIM-supported Zif-8 nanoparticles as shown in Figure 12.

The nitrogen adsorption-desorption isotherms display typical reversible type I isotherms with very little hysteresis. The rapid increase in the adsorbed N₂ at low pressures suggests the presence of a microporous structure. Furthermore, the hysteresis loop at high-pressure ratios indicates the existence of interparticle mesoporosity and macroporosity between Zif-8 particles. The specific surface area and the pore volume of the prepared PIM-supported Zif-8 were 1114.5 m² g⁻¹ and 0.83 cm³ g⁻¹. The pore size distribution (PSD) curve shows that the samples exhibit a dominant pore diameter of approximately 1.01 nm. These results are mainly in agreement with data in the literature, and some differences are mainly due to the different synthesis conditions.

5.2. Gas Transport Characteristics of the Membranes. The pure gas permeability and ideal selectivity measurements of PIM-co-MOF and neat PIM are represented for two temperatures (25 and 50 °C) in Figure 13.

As can be seen from the figures, with the temperature increase, the gas permeability in both types of membranes slightly increases for all gas species with an order CO₂ > CH₄ > N₂. However, the increase in the permeation rate with increasing temperature is more pronounced, for the less permeable species, i.e., N₂ and then CH₄. The literature review shows that, with increasing temperature, the permeation rate increases in the polymer inclusion membranes, while it decreases in the Zif-8 membranes [8, 24]. Therefore, the increasing trends of data show that the polymer inclusion membrane layer is the determinant and limiting factor in the permeation rate. The next thing to note is that the neat PIM exhibited significantly higher gas permeability than PIM-co-MOF. This reveals that the continuous coverage of the membrane surface by Zif-8 caused an almost 50% permeability reduction compared to neat PIM. Gas permeation through the PIM-co-MOF membrane can be explained by a combination of two mechanisms including the solution-diffusion and adsorption-diffusion mechanisms. This means that gas molecules firstly adsorb on the MOF layer, then undergo a Knudsen diffusion through MOF channels, next dissolve in polymer inclusion membrane, reach PIM surface

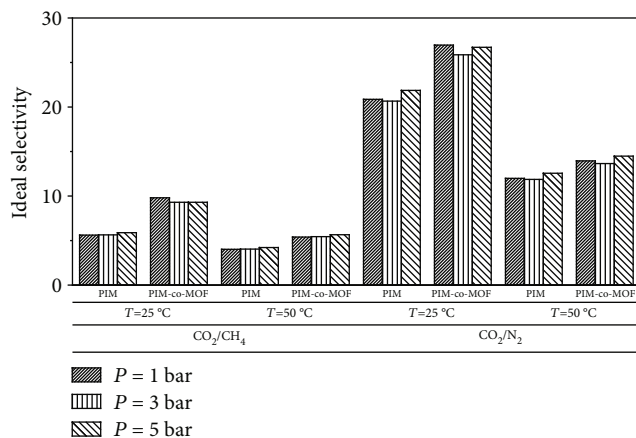


FIGURE 14: Permselectivity of PIM and PIM-co-MOF at two temperatures and different pressures.

and diffuse through, and finally desorb at the other side of the membrane. With increasing temperature, the molecular motions in PIM increase, and subsequently, the solution and diffusion of gas species are increased while gas adsorption on the surface of Zif-8 layer is decreased especially for CO₂. Therefore, the gas permeability decreased in MOF membranes. As a result of these two events, the gas permeability of PIM-co-MOF will not increase as much as that of PIM.

Moreover, it can be seen from the figures that gas permeation rates increase slightly with the increasing feed pressure. With increasing feed pressure, on the one hand, viscous flow and Knudsen diffusion increase considerably in the MOF layer, and on the other hand, the membrane-free volumes decrease, exerting an opposite effect on the permeation of gases over PIM-co-MOF membrane. Therefore, no significant change in permeability (especially for N₂ in which the permeation was more influenced by the membrane compaction) is observed. Overall, N₂ and CH₄ hardly pass through the membrane by a solution-diffusion mechanism, while CO₂ transport behavior is according to an adsorption-controlled transport [8]. Figure 14 compares the effect of feed pressure on CO₂/CH₄ and CO₂/N₂ permselectivity over both types of membranes at two temperatures of 25 and 50 °C.

A comparison of permselectivity data indicates that a slight increase in both CO₂/CH₄ and CO₂/N₂ ideal selectivity is observed with increasing feed pressure which could be attributed to a relatively larger increase in CO₂ permeability than N₂ and CH₄ permeability when the pressure increased. Although the same trend of selectivity values with the temperature has been observed for both types of membranes, ideal permselectivity values measured for PIM-co-MOF membrane are higher than those calculated in neat PIM.

Although the value of CO₂ permeability is reduced by an average of 21%, with the crystal growth of Zif-8 nanoparticles on the surface of the polymer inclusion membrane, the CO₂/N₂ and CO₂/CH₄ gas selectivity of membranes following the adsorption-diffusion mechanism increased significantly. As can be seen, the CO₂/N₂ and CO₂/CH₄ selectivity at 50 °C increases which could be attributed to the carrier-mediated diffusion mechanism for the CO₂ transport through PIMs, similar to what was reported by Kebiche-

Senhadji et al. Crown ether as the carrier could react with CO₂ in a reversible complexation form, and consequently, total CO₂ flux is originated from the facilitated transport of the carrier-CO₂ complex and the simple diffusion of CO₂.

6. Conclusions

Zif-8 is successfully anchored onto the surface of amino-functionalized PIM configured into a flat-sheet membrane module during the process of ligand extraction. The different characterization techniques confirmed the growth of a thick and continuous layer of Zif-8 on aminosilane-modified PIM. According to the observations, we assumed that the MOF's crystalline layer could not grow well on the neat PIM surface. The gas transport behavior of both the neat PIM and PIM-co-MOF was measured using pure CO₂, N₂, and CH₄ gases at the different temperatures and pressures. The growth of the Zif-8 nanoparticle layer on the modified PIM leads to a dramatic increase in selectivity and a slight decrease in gas permeability. The membranes have the same permeation rate order CO₂ > CH₄ > N₂. The permeability in both types of membranes increases with increasing temperature for three gases. This increase is much more significant in the case of neat PIM compared to PIM-co-MOF. As the temperature increases, the CO₂/N₂ and the CO₂/CH₄ selectivity in both cases decrease which is slightly more pronounced for the case of PIM-co-MOF. The results revealed no significant effect of feed pressure on permeability. The DFT study shows that the Zif-8 compound has a metallic behavior, and the tendency of this compound to adsorption of CO₂ molecules is greater than in other cases. Also, the optical calculation of DFT simulations confirmed that the Zif-8+CO₂ is chosen for optical infrared applications due to its higher adsorption coefficient. These results prove the agreement between experiment and theory. This work provides guidelines for rational design of MOF-covered-polymer inclusion membranes for gas separation application or as sensing materials for the detection of combustion gases.

Data Availability

The data used to support the findings of this study are available from the corresponding author upon request.

Conflicts of Interest

The authors declare that they have no conflicts of interest.

Acknowledgments

This work is supported by the faculty of petroleum and gas, Yasouj University, Gachsaran, Iran (75813-56001) and the Dena High-Performance Computing (HPC) of Yasouj University.

References

- [1] H. Adelnia, H. C. Bidsorkhi, A. F. Ismail, and T. Matsuura, "Gas permeability and permselectivity properties of ethylene vinyl acetate/sepiolite mixed matrix

- membranes,” *Separation and Purification Technology*, vol. 146, pp. 351–357, 2015.
- [2] M. S. Jyothi, K. R. Reddy, K. Soontarapa et al., “Membranes for dehydration of alcohols via pervaporation,” *Journal of Environmental Management*, vol. 242, pp. 415–429, 2019.
- [3] A. Ali, R. A. Tufa, F. Macedonio, E. Curcio, and E. Drioli, “Membrane technology in renewable-energy-driven desalination,” *Renewable and Sustainable Energy Reviews*, vol. 81, pp. 1–21, 2018.
- [4] M. I. G. S. Almeida, A. M. L. Silva, R. A. Coleman, V. J. Pettigrove, R. W. Cattrall, and S. D. Kolev, “Development of a passive sampler based on a polymer inclusion membrane for total ammonia monitoring in freshwaters,” *Analytical and Bioanalytical Chemistry*, vol. 408, no. 12, pp. 3213–3222, 2016.
- [5] R. Darvishi, J. k. Sabet, and M. N. Esfahany, “Preparation and characterization of a novel calcium-conducting polymer inclusion membrane: Part I,” *Korean Journal of Chemical Engineering*, vol. 35, no. 10, pp. 2052–2064, 2018.
- [6] B. Kuswandi, F. Nitti, M. I. G. S. Almeida, and S. D. Kolev, “Water monitoring using polymer inclusion membranes: a review,” *Environmental Chemistry Letters*, vol. 18, no. 1, pp. 129–150, 2020.
- [7] F. A. Tabr, F. Salehiravesh, H. Adelnia, J. N. Gavgani, and M. Mahyari, “High sensitivity ammonia detection using metal nanoparticles decorated on graphene macroporous frameworks/polyaniline hybrid,” *Talanta*, vol. 197, pp. 457–464, 2019.
- [8] M. A. Carreon, *Membranes for gas separations*, World Scientific, 2017.
- [9] C. Chen, A. Ozcan, A. O. Yazaydin, and B. P. Ladewig, “Gas permeation through single-crystal ZIF-8 membranes,” *Journal of Membrane Science*, vol. 575, pp. 209–216, 2019.
- [10] Y.-W. Jeon and D.-H. Lee, “Gas Membranes for CO₂/CH₄ (Biogas) Separation: A Review,” *Environmental Engineering Science*, vol. 32, no. 2, pp. 71–85, 2015.
- [11] R. Khalilpour, K. Mumford, H. Zhai, A. Abbas, G. Stevens, and E. S. Rubin, “Membrane-based carbon capture from flue gas: a review,” *Journal of Cleaner Production*, vol. 103, pp. 286–300, 2015.
- [12] S. H. Amaley, R. S. Sapkal, and V. S. Sapkal, “Pervaporation: A Novel Process for Ethanol Separation using Fermentation,” *International Journal of Engineering Research*, vol. 4, no. 2, pp. 64–68, 2015.
- [13] K. Goh, H. E. Karahan, E. Yang, and T.-H. Bae, “Graphene-Based Membranes for CO₂/CH₄ Separation: Key Challenges and Perspectives,” *Applied Sciences*, vol. 9, no. 14, p. 2784, 2019.
- [14] S. Friebe, L. Diestel, A. Knebel, A. Wollbrink, and J. Caro, “MOF-Based Mixed-Matrix Membranes in Gas Separation - Mystery and Reality,” *Chemie Ingenieur Technik*, vol. 88, no. 11, pp. 1788–1797, 2016.
- [15] O. Kebiche-Senhadji, S. Bey, G. Clarizia, L. Mansouri, and M. Benamor, “Gas permeation behavior of CTA polymer inclusion membrane (PIM) containing an acidic carrier for metal recovery (DEHPA),” *Separation and Purification Technology*, vol. 80, no. 1, pp. 38–44, 2011.
- [16] T. T. Rodenas, M. van Dalen, E. García-Pérez et al., “Visualizing MOF Mixed Matrix Membranes at the Nanoscale: Towards Structure-Performance Relationships in CO₂/CH₄-Separation Over NH₂-MIL-53(Al)@PI,” *Advanced Functional Materials*, vol. 24, no. 2, pp. 249–256, 2014.
- [17] M. Pakizeh, S. Ofoghi, and S. H. R. Shooshtari, “Modeling of gas permeation through mixed matrix membranes using a comprehensive computational method,” *Korean Journal of Chemical Engineering*, vol. 33, no. 11, pp. 3194–3202, 2016.
- [18] Z.-c. Gao, L.-q. Li, H.-l. Li, R.-f. Chen, S. Wang, and Y.-g. Wang, “A hybrid zeolitic imidazolate framework Co-IM-mIM membrane for gas separation,” *Journal of Central South University*, vol. 24, no. 8, pp. 1727–1735, 2017.
- [19] H. A. Ozen and B. Ozturk, “Gas separation characteristic of mixed matrix membrane prepared by MOF-5 including different metals,” *Separation and Purification Technology*, vol. 211, pp. 514–521, 2019.
- [20] E. Barankova, X. Tan, L. F. Villalobos, E. Litwiller, and K. V. Peinemann, “A metal chelating porous polymeric support: the missing link for a defect-free metal-organic framework composite membrane,” *Angewandte Chemie International Edition*, vol. 56, no. 11, pp. 2965–2968, 2017.
- [21] A. Fuoco, M. Khdhayyer, M. Attfield, E. Esposito, J. Jansen, and P. Budd, “Synthesis and Transport Properties of Novel MOF/PIM-1/MOF Sandwich Membranes for Gas Separation,” *Membranes*, vol. 7, no. 1, p. 7, 2017.
- [22] J. Hou, P. D. Sutrisna, Y. Zhang, and V. Chen, “Formation of ultrathin, continuous metal-organic framework membranes on flexible polymer substrates,” *Angewandte Chemie International Edition*, vol. 55, no. 12, pp. 3947–3951, 2016.
- [23] L. Ma, F. Svec, T. Tan, and Y. Lv, “In-situ growth of highly permeable zeolite imidazolate framework membranes on porous polymer substrate using metal chelated polyaniline as interface layer,” *Journal of Membrane Science*, vol. 576, pp. 1–8, 2019.
- [24] K. R. Reddy, H. M. Jeong, Y. Lee, and A. V. Raghun, “Synthesis of MWCNTs-core/thiophene polymer-sheath composite nanocables by a cationic surfactant-assisted chemical oxidative polymerization and their structural properties,” *Journal of Polymer Science Part A: Polymer Chemistry*, vol. 48, no. 7, pp. 1477–1484, 2010.
- [25] Y. Zhang, X. Feng, S. Yuan, J. Zhou, and B. Wang, “Challenges and recent advances in MOF-polymer composite membranes for gas separation,” *Inorganic Chemistry Frontiers*, vol. 3, no. 7, pp. 896–909, 2016.
- [26] L. S. Lai, Y. F. Yeong, T. L. Chew, K. K. Lau, and M. S. Azmi, “CO₂ and CH₄ gas permeation study via zeolitic imidazolate framework (ZIF)-8 membrane,” *Journal of Natural Gas Science and Engineering*, vol. 34, pp. 509–519, 2016.
- [27] P. Giannozzi, S. Baroni, N. Bonini et al., “QUANTUM ESPRESSO: a modular and open-source software project for quantum simulations of materials,” *Journal of Physics: Condensed Matter*, vol. 21, no. 39, article 395502, 2009.
- [28] J. P. Perdew, K. Burke, and M. Ernzerhof, “Generalized Gradient Approximation Made Simple,” *Physical Review Letters*, vol. 77, no. 18, pp. 3865–3868, 1996.
- [29] H. J. Monkhorst and J. D. Pack, “Special points for Brillouin-zone integrations,” *Physical Review B*, vol. 13, no. 12, pp. 5188–5192, 1976.
- [30] P. K. Misra, “Basic properties of crystals,” in *Physics of Condensed Matter*, P. K. Misra, Ed., pp. 1–35, Elsevier, Boston, 2012.
- [31] T. Rangel, D. Kecik, P. E. Trevisanutto, G. M. Rignanese, H. Van Swygenhoven, and V. Olevano, “Band structure of gold from many-body perturbation theory,” *Physical Review B*, vol. 86, no. 12, 2012.
- [32] S. U. Hong, S. P. Singh, M. Pyo, W. B. Park, and K.-S. Sohn, “Density functional theory calculations for the band gap and

- formation energy of $\text{Pr}_{4-x}\text{Ca}_x\text{Si}_{12}\text{O}_{3+x}\text{N}_{18-x}$; a highly disordered compound with low symmetry and a large cell size," *Physical Chemistry Chemical Physics*, vol. 19, no. 25, pp. 16702–16712, 2017.
- [33] F. Wooten, "Maxwell's equations and the dielectric function," in *Optical Properties of Solids*, F. Wooten, Ed., pp. 15–41, Elsevier, 1972.
- [34] S. L. Adler, "Quantum Theory of the Dielectric Constant in Real Solids," *Physical Review*, vol. 126, no. 2, pp. 413–420, 1962.
- [35] V. Lucarini, J. J. Saarinen, K.-E. Peiponen, and E. M. Vartiainen, *Kramers-Kronig relations in optical materials research*, Springer Science & Business Media, 2005.
- [36] E. Pakizeh and M. Moradi, "Effect of particle size on the optical properties of lead zirconate titanate nanopowders," *Journal of the American Ceramic Society*, vol. 101, no. 12, pp. 5335–5345, 2018.
- [37] E. Pakizeh, J. Jalilian, and M. Mohammadi, "Electronic, optical and thermoelectric properties of Fe_2ZrP compound determined via first-principles calculations," *RSC Advances*, vol. 9, no. 44, pp. 25900–25911, 2019.
- [38] P.-S. Wei, Y.-C. Hsieh, H.-H. Chiu et al., "Absorption coefficient of carbon dioxide across atmospheric troposphere layer," *Heliyon*, vol. 4, no. 10, article e00785, 2018.
- [39] T. E. Klimeshina, T. M. Petrova, O. B. Rodimova, A. A. Solodov, and A. M. Solodov, "CO₂ absorption in band wings in near IR," *Atmospheric and Oceanic Optics*, vol. 28, no. 5, pp. 387–393, 2015.
- [40] A. Soleimany, J. Karimi-Sabet, and S. S. Hosseini, "Experimental and modeling investigations towards tailoring cellulose triacetate membranes for high performance helium separation," *Chemical Engineering Research and Design*, vol. 137, pp. 194–212, 2018.